Journal of ELECTRONIC MATERIALS, Vol. 48, No. 4, 2019
https://doi.org/10.1007/s11664-019-06951-y

TiO_2 Nanotubes with Nanograss Structure: The Effect of the Anodizing Voltage on the Formation Mechanism and Structure Properties

HENIA FRAOUCENE,[1,4] DJEDJIGA HATEM,[1] FLORENCE VACANDIO,[2] and MARCEL PASQUINELLI[3]

1.—Laboratory of Advanced Technologies of Genie Electrics (LATAGE), Faculty of Electrical and Computer Engineering, Mouloud Mammeri University (UMMTO), BP 17 RP, 15000 Tizi-Ouzou, Algeria. 2.—UMR 7246 Matériaux Divisés, Interfaces, Réactivité, Electrochimie (MADIREL), Aix Marseille Université, St Jérôme Center, Traverse Susini, 13397 Marseille Cedex 20, France. 3.—UMR 7334 Institute of Microelectronic Materials Nanosciences of Provence (IM2NP), Optoelectronics and Photovoltaics (OPTO-PV) Team, Aix Marseille Université, Faculty of St Jérôme, Avenue Escadrille Normandie Niemen, 13397 Marseille Cedex 20, France. 4.—e-mail: fraoucene.henia@yahoo.com

Titanium dioxide nanotubes (TiO_2 NTs) with a nanograss structure were synthesized in a fluoride organic electrolyte based on ethylene glycol under a potentiostatic anodization regime. By varying the anodization voltage, significant morphological differences were obtained, and the upper NTs' surface has a nanograss appearance caused by the thinning of top tube walls, the result of the vertical splitting mechanism of nanograss growth. The samples were characterized using techniques such as scanning electron microscopy, x-ray diffraction, UV–visible spectroscopy and Mott–Schottky (MS) analysis. The obtained results show that samples annealed at 500°C for 3 h crystallized into anatase form and displayed the apparition of rutile phase at higher anodization voltage, where the morphology was significantly improved with thicker tube walls. The MS measurement of all samples displays a *n*-type semiconductor nature and the flat band potential (U_{fb}) takes less negative values by the increasing anodization voltage. As a result, TiO_2 NTs with a nanograss structure expedite electron–hole separation, therefore, providing a lower recombination rate.

Key words: TiO_2 nanotubes, nanograss, anodization process, properties, nanomaterials

INTRODUCTION

Titanium dioxide (TiO_2) is a semiconductor material that has been studied extensively in the last few decades due to its chemical stability, nontoxicity and biocompatibility.[1–3] To diversify the technological applications of TiO_2, researchers have sought to reduce the size of TiO_2 to the nanometer scale to increase not only the number of reaction sites but also to give new properties to the material.[4] Synthesis of nanotubes (NTs) and other one-dimensional TiO_2 nanostructures (e.g., nanowires, nanodots and nanorods) may be achieved through various processes including hydrothermal synthesis,[5] template-assisted[6] and anodic-oxidation.[7–11] Among these processes, electrochemical anodization of titanium (Ti) in aqueous and organic solutions containing fluoride ions has been known as a very simple and controllable method to fabricate highly ordered TiO_2NTs arrays.[12] Assefpour–Dezfuly[13] and Zwilling et al.[14] were the first to report the formation of TiO_2 porous films by the anodization of Ti foil in chromic acid (CA) (0.5 mol l^{-1} Cr_2O_3)

(Received March 7, 2018; accepted January 9, 2019; published online January 18, 2019)

solution with or without hydrofluoric acid (HF) (9.5×10^{-2} mol 1^{-1}) addition. A decade later, Gong et al.[15] first reported the formation of uniform TiO_2 NTs arrays via anodic oxidation of Ti in a hydrofluoric acid (HF) electrolyte. Recently, the Schmuki group[16,17] also reported the formation of long NTs during anodization of Ti in neutral fluoride solutions. Self-organized TiO_2 NTs are used in various fields, such as dye sensitized solar cells,[18–21] sensors,[22] photocatalysis[23–26] and biomedical applications.[27] Some applications require the use of longer tubes, anodization in fluoride solutions for longer duration addresses this problem. The inconvenience of this process is that the top surface of TiO_2 NTs has a nanograss character caused by the thinning of the upper part of the tube walls.[28] The formation mechanism of nanograss is not very well understood, and is restricted to the etching (chemical dissolution) of the top part of the tube after a long anodization duration. Naduvath et al.[29] have studied the effect of water content in electrolyte on nanograss formation upon TiO_2 NTs arrays resulting in different morphologies type "viz ring" or "vertical" splitting. Lim et al.[30] have reported the synthesis of TiO_2 nanowires by the anodization of Ti foil in a fluoride organic solution based on the bamboo-splitting model.

Furthermore, the soaking of as-anodized TiO_2 NTs in water or acid solutions for a long time leads to a change in geometry of TiO_2 NTs. Zhang et al.[31] have developed rough TiO_2 NTs arrays by soaking the prepared TiO_2 NTs in water for 80 h at room temperature. The result showed an increase in specific surface area that exhibits a very high average specific capacitance of 20.96 mF cm^{-2} at a current density of 0.05 mA cm^{-2} after an electrochemical hydrogenation doping process. Wang et al.[32] have demonstrated the morphology transformation of the as-anodized TiO_2 NTs upon water soaking from a nanotubular structure to anatase mesoporous TiO_2 nanowires that showed an enhanced photocatalytic activity toward hydrogen evolution, up to 1.9 times higher than annealed anatase TiO_2 NTs. However, Zhao et al.[33] have synthesized TiO_2 NTs covered with nanograss by soaking in H_3PO_4 and hydrogenation doping. They showed that the TiO_2 nanograss structure improved the areal capacitance by up to 67.7%, and it is still up to 23.5% higher than of TiO_2 NTs without nanograss after 2000 cycles. In the same way, Du et al.[34] have reported an improvement of electrochemical capacitance by up to 43.4% arising from the specific surface area of well-aligned TiO_2 NTs arrays with a nanograss structure.

In this work, we examined the influence of anodization voltage on the obtained TiO_2 NTs covered with a nanograss layer on top of the tubes under a potentiostatic anodization regime. The mechanism of nanograss appearance over TiO_2 NTs has been described based on a vertical splitting model. The morphological, structural, optical and semiconducting properties of TiO_2 NTs with nanograss structure were investigated by scanning electron microscope (SEM), x-ray diffraction (XRD), UV–visible spectroscopy and Mott–Schottky (MS) analysis.

EXPERIMENTAL

Substrate Preparation

The Ti foil (0.25 mm, 99.5% purity, Sigma-Aldrich) was cut into a square shaped piece (1.5 cm × 1.5 cm) with a selected work area of 0.6 cm^2. Before anodization the samples must have a smooth and clean surface to avoid any adhesion problems at the TiO_2/Ti interface. Firstly, the substrates were subjected to a polishing using a rotating felt mat (0.1 μm) impregnated with alumina until a mirror-like surface was obtained. Subsequently, the substrates were degreased by sonication in acetone, methanol and 2-propanol for 10 min, respectively. The treatment in an ultrasonic bath involves combining the action of ultrasonic vibrations with that of solvents in order to degrease the surface and to remove any foreign matter or impurities from the mechanical polishing step. Finally the substrates were rinsed with ultrapure water and dried in a stream of compressed air.

Synthesis of TiO_2 Nanotubes

To obtain TiO_2 NTs with nanograss structures, we opted for the use of an anodization process which is a very simple and controllable method. Figure 1 describes the potentiostatic anodization system used for the electrochemical experiments. A conventional two-electrode cell was used for all the anodization measurements, a platinum foil (2.5 cm^2) served as the counter electrode (cathode) and Ti as the working electrode (anode) is in contact with a Cu-ring containing an O-ring to prevent electrolyte losses and then pressed with a seal into the wall of the electrochemical cell. The distance between the electrodes was 20 mm. The system power supply was assured using a PARSTAT 2273 potentiostat/galvanostat that delivered a maximum voltage of 10 V which will be multiplied by ten (× 10) using a potentiometer (divider bridge) connected to the cell. The electrochemical system is assisted by a computer-controlled software POWER SUITE in order to visualize electrochemical characterization results (for example: current–time curves). The anodization solution was ethylene glycol (EG) ($HOCH_2CH_2OH$) containing 0.3 wt.% ammonium fluorides (NH_4F) and 2 wt.% ultrapure water. The samples were anodized at room temperature for 3 h by varying the anodizing voltage (20, 40 and 60 V). The selection of these anodization voltages comes down to the importance and the effect of these voltages on the structure and morphological parameters of TiO_2 NTs, notably the tubes' diameter. In other studies,[35,36] researchers

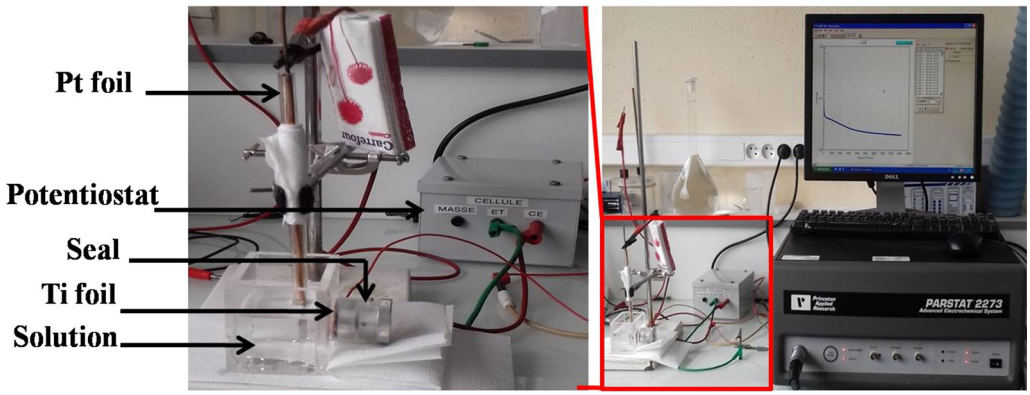

Fig. 1. Potentiostatic anodization system used for the electrochemical experiments.

have synthesized TiO_2 NTs using similar anodization voltages but for shorter anodization times. As a result, they have not obtained nanograss structures. In light of this, the present study aims to investigate the influence of the anodization voltage on the growth of TiO_2 NTs with nanograss structures for extended anodization times.

After anodization, the samples were soaked in ultrapure water for 10 min and then dried in an oven at 50°C for 10 min. In order to transform the amorphous crystallographic structure obtained just after electrochemical anodization into a crystalline structure, the samples were annealed at 500°C for 3 h with a heating and cooling rate of 5°C/min. The heat treatment at 500°C for 3 h makes it possible to crystallize the samples into anatase form. The anatase structure has been identified as the most effective variety among all crystalline forms of TiO_2. This is attributed mainly to the width of the band gap and higher conduction band-edge energy, making it optically active to different radiation energies, and allowing an improvement of the mobility of the charges created in the semiconductor under the impact of absorbed photons. Such properties make anatase phase TiO_2 useful for a variety of applications, such as in dye-sensitized solar cells, photocatalysis and Li^+ batteries.[37,38]

Characterization of the Samples

Morphological characterization of the TiO_2 NTs was carried out using SEM. The average length of TiO_2 NTs was determined directly based on cross-sectional images after cleaving the samples. The crystalline phases were characterized by XRD analysis performed with an X' pert Philips MPD with a Panalytical X'celerator detector using graphite monochromized CuKα radiation (λ = 1.5418 Å). The measurements were performed within the 2θ range from 20° to 70°. The optical properties were investigated using UV spectroscopy over the wavelength range covering 250–750 nm. The electrochemical tests were carried out in a conventional three-electrode cell, with an AgCl/KCl bar used as the reference electrode, a platinum bar as the counter electrode and TiO_2 films as the working electrodes. All experiments were carried out at room temperature with a signal frequency value of 1 kHz in ammonium sulfate $(NH_4)_2SO_4$ (1 M/L) electrolyte at open circuit potential. The semiconducting properties of the TiO_2 NTs with nanograss layers such as the semiconducting type, the donor concentration (N_d) and the flat band potential (U_{fb}) were estimated from MS plots. The relationship between C_{sc} and U is given by the following MS equation[39]:

$$C_{sc}^{-2} = \left(\frac{2}{e\varepsilon\varepsilon_0 N_d}\right)\left(U - U_{fb} - \frac{KT}{e}\right), \qquad (1)$$

where C_{sc}^{-2} is the differential capacitance of the space-charge region, k Boltzmann's constant (1.38×10^{-23} J K^{-1}), ε_0 the vacuum permittivity of free space (8.854×10^{-12} F m^{-1}), e the elementary charge (1.6×10^{-19} C), ε the dielectric constant of TiO_2 (here, the following values were considered: 50 for anatase, 100 for rutile and 38 for amorphous[39,40]), N_d the donor density or carrier concentration, U applied potential, U_{fb} the flat-band potential, and kT/e is about 25 mV at ambient temperature.

EXPERIMENTAL RESULTS

Morphological Characterization

Figure 2 displays the surface morphology of Ti surfaces after the anodizing process under applied voltages of 20 V, 40 V and 60 V for 3 h. Several topological characteristics of the anodized surfaces exist including thickness, diameter, length of nanotubes and apparition of the nanograss aspect. At the voltage of 20 V (Fig. 2a), the surface of the TiO_2 NTs was markedly covered with nanograss structures following the formation of beams from the remainder of the tubes after a long period of anodizing. Also at 40 V, the nanograss form was always present over the nanotubular structure with the presence of some initiation layer distinct from

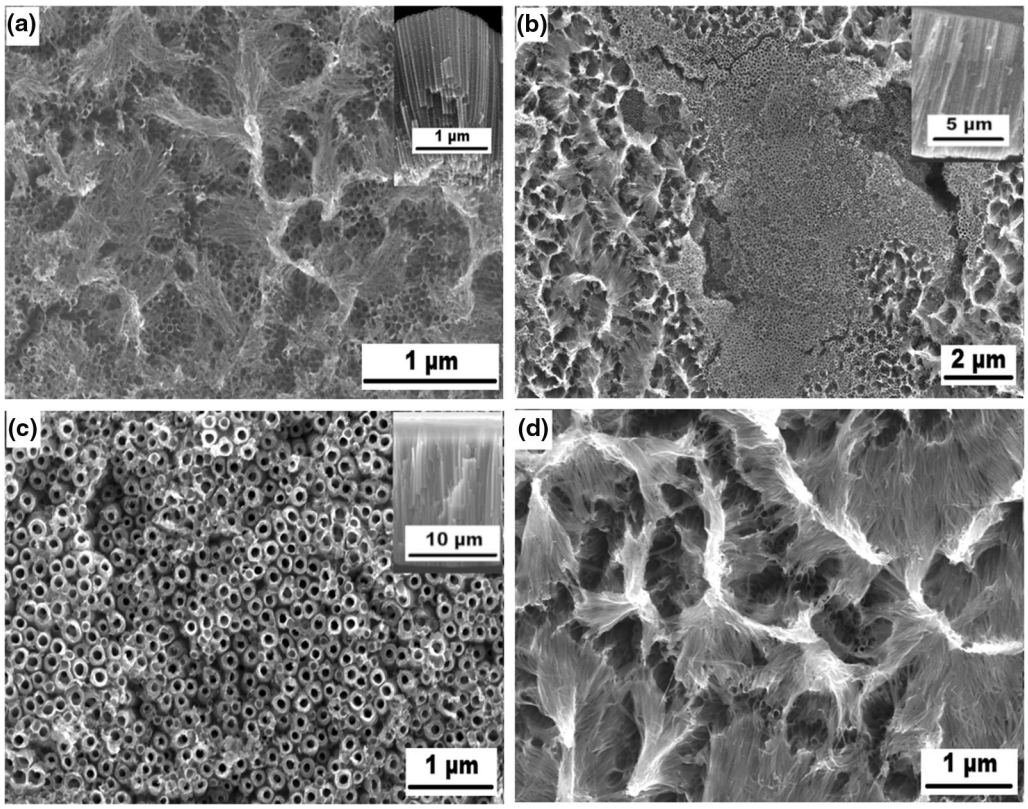

Fig. 2. SEM images of TiO_2NTs with nanograss layer anodized in fluoride organic solutions for 3 h at: (a) 20 V, (b) 40 V and (c) 60 V (cross-sectional SEM views of films shown in inset), (d) SEM view of TiO_2 NTs with nanograss attached to its NTs source formed at 40 V.

the nanograss itself (see Fig. 2b). On the other hand, nanograss appearance was significantly diminished at 60 V, and the tubes' walls were thickened (Fig. 2c). Furthermore, an important enhancement of the tubes' lengths is noted with an increase in the applied voltage, namely 2 μm, 10.8 μm and 16.1 μm lengths are observed for films prepared at 20 V, 40 V and 60 V, respectively (see the insets in Fig. 2). According to the literature,[41–43] the basic mechanism for the formation of TiO_2 NTs during the anodization process is competition between TiO_2 formation and chemical dissolution of this oxide. Firstly, an oxide layer grows on the Ti surface due to the interaction of metallic cations Ti^{4+} (generated by anodic oxidation of Ti foil, reaction (2) below) with oxygen ions O^{2-} or OH^- present in the electrolyte from the reduction of H_2O at the counter electrode (reaction (3)), which can be considered uniformly distributed over the entire surface. The overall reaction is known as a hydrolysis reaction (reaction (4)).

$$Ti \rightarrow Ti^{4+} + 4e^- \quad (2)$$

$$4H_2O + 4e^- \rightarrow 2H_2 + 4OH^- \quad (3)$$

$$Ti + 2H_2O \rightarrow TiO_2 + 4H^+ \quad (4)$$

Once the oxide layer is formed, O^{2-} anions migrate through the TiO_2 layer under the applied electric field to the Ti/TiO_2 interface for a further reaction with Ti. At the same time, Ti^{4+} cations migrate from the Ti/TiO_2 interface towards the oxide/electrolyte. Also, the TiO_2 layer being in contact with the fluorinate electrolyte, it will be etched by F^- ions through chemical dissolution to form soluble fluoride complexes $[TiF_6]^{2-}$ (reaction (5)).

$$Ti^{4+} + 6F^- \rightarrow [TiF_6]^{2-} \quad (5)$$

$$TiO_2 + 6F^- + 4H^+ \rightarrow [TiF_6]^{2-} + 2H_2O \quad (6)$$

Finally, the oxide layer is locally dissolved and NTs are created from small pits that grow into bigger pores with increasing anodization time to form a tube (reaction (6)). When an electrochemical equilibrium achieved between electrochemical etching and chemical dissolution of TiO_2, the tubes' lengths remain unchanged.[44,45] For a long anodizing time, chemical etching takes place on the top walls of the tubes and the upper morphology has a nanograss appearance. Thereby, the apparition of this structure marks the end of the anodization process.

The diffusion rate of the species present in the electrolyte such as F^- and $[TiF_6]^{2-}$ is proportional to the anodizing voltage. At low anodizing voltages,

the low diffusion of fluoride ions through the porous layer results in inhomogeneous distribution along the tube walls. This phenomenon results in mechanical defects appearing along the formed thin tubes walls ensuring the existence of etchings sites yielding the formation of the fluoride complex $[TiF_6]^{2-}$). This complex enhances electrochemical etching and cracks appear giving vertical splitting of the tube resulting in the bending and collapsing of TiO_2 NTs leading to a nanograss aspect. This means that the nanograss layer has the NTs as its source and so is attached to them, as can be seen in Fig. 2d. The same nanograss formation mechanism is proposed by Naduvath et al.,[29] Lim et al.,[30] Wu et al.[46] and Wang et al.[47] where the nanograss layer could be produced by optimizing the electrolyte solution content and anodizing time.

Under rapid potensiostatic anodization (60 V), the morphology of TiO_2 NTs was markedly improved and the nanograss was significantly eliminated (partially with some debris) with a tube diameter of 106 nm approximately. This can be explained by the high potential negating the high viscosity of the organic solutions (ethylene glycol has a viscosity of 16.1 cP[48]) and favoring the diffusion of the species present in the solution wherever the concentration of $[TiF_6]^{2-}$ increases near initial crack sites, thus inhibiting the formation of new cracks.

Figure 3 shows the current/time response of TiO_2 NTs formed at different anodization voltages. For all the anodizing voltages, the same behavior is observed showing the different stages of TiO_2 NTs growth. In step (I), the current at 60 V is much higher (14 mA) characterized by a sharp drop, enabling horizontal growth of the pores.[49] This result is in agreement with the morphology obtained from SEM as can be seen in Fig. 2c. In step (II), a small increase in current occurs (see the inset in Fig. 3) and irregular pores are initially formed on the TiO_2 layer by the formation of soluble $[TiF_6]^{2-}$ complexes. In step (III), the currents had fixed values as signed by the formation of TiO_2 NTs with nanograss layer.

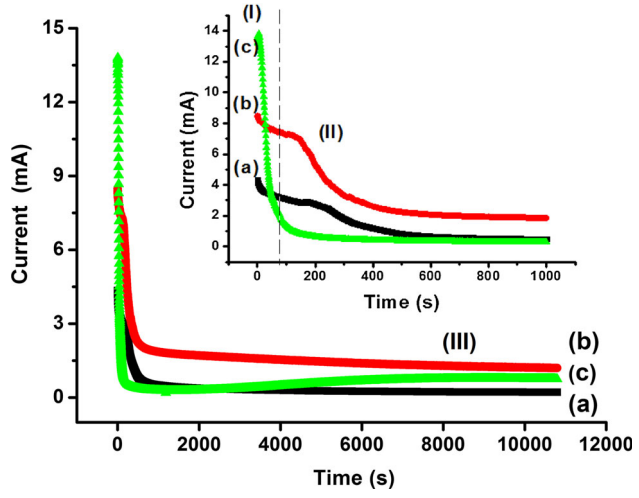

Fig. 3. *I-t* curves of anodized samples in fluoride organic solution for 3 h at: (a) 20 V, (b) 40 V and (c) 60 V, (*I-t* curve evolution in the second region shown in inset).

Structural Properties

After anodization, the TiO_2 NTs with nanograss layers were annealed at 500°C for 3 h to convert the

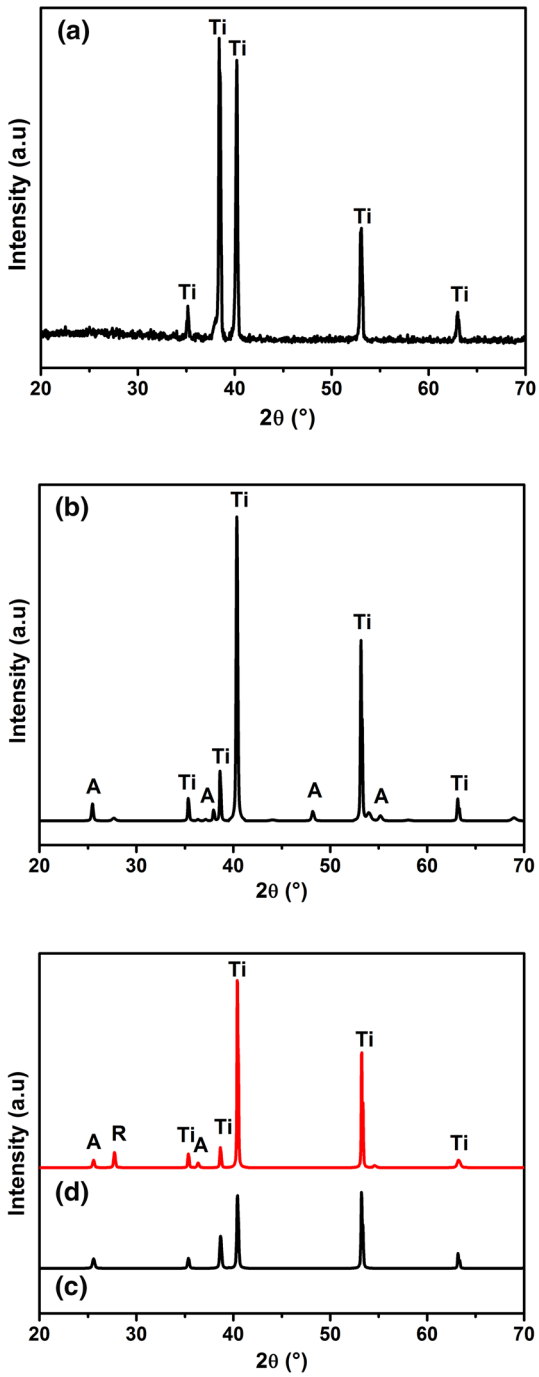

Fig. 4. XRD pattern of the as-anodized film (a), XRD patterns of annealed films at 500°C for 3 h synthesized at: 40 V (b), 20 V (c) and 60 V (d).“A” is anatase, “R” is rutile. “Ti” is substrate–film.

amorphous structure into a crystalline structure. Figure 4 shows the XRD patterns of these films. Compared with the amorphous structure obtained just after anodization (as-anodized) (Fig. 4a), the crystalline structures of these films are mainly the anatase phase, as evidenced by the strong diffraction peaks at 2θ = 25.55°, 36.34°, 37.94°, 48.16° and 55.21°, which can be indexed to the (101), (103), (004), (200) and (211) planes, respectively (JCPDS Pattern no 00-021-1272). This result is in accordance with the study of Wu et al.[46] where an anatase phase is obtained for different types of TiO_2 nanowires synthesized using an anodization process in an EG electrolyte containing 0.2 wt.% HF and 0.3 wt.% water at 100 V for 3 h. By increasing the anodizing voltage to 60 V (Fig. 4d), the rutile phase begins to appear as evidenced by the diffraction peak (2θ = 27.71°), linked to the crystal face (110) (JCPDS Pattern no 00-021-1276). This behavior could be due to the fact that TiO_2 NTs are thickened by increasing the anodization voltage, such that the TiO_2 NTs' morphology was markedly improved and the nanograss was significantly removed as observed in the SEM image (Fig. 2c). In addition, the beginning of reorientation of the Ti–O bond in thick TiO_2 NTs walls to form a stable rutile phase can cause the appearance of a rutile peak with a low intensity compared to the anatase peaks indicating that the anatase phase is relatively predominant. Varghese et al.[50] obtained the rutile phase in GAXRD patterns near 430°C for TiO_2 NTs annealed for 3 h and synthesized in 0.5 vol.% hydrofluoric acid at 20 V for 45 min. Furthermore, many studies explain the apparition of rutile phase by the growth of a new oxide layer (TiO_2) along the tubes' walls from oxidation of Ti foil.[51,52]

Optical Properties

Figure 5 shows the optical absorption spectra of annealed TiO_2 NTs with nanograss layers. The strongest absorption in these films is in the range of 250–360 nm. The band gap absorption edges of crystalline TiO_2 NTs with nanograss layers obtained at 20 V and 40 V are around 355 nm and 370 nm, respectively, which are close to the band gap absorption edge of anatase TiO_2, with band gap energy of 3.23 eV.[53] Furthermore, an extended absorption band was found in the visible region (around 400 nm) for films prepared at 60 V. Samples synthesized under rapid potensiostatic anodization show an improved morphology owing to the prevention of the formation of the nanograss layer, as confirmed by the SEM image in (Fig. 2c) and the apparition of the rutile phase in the XRD pattern (Fig. 4d). In the same context, Wu et al.[46] found a strong light absorption in the visible range of TiO_2 nanowires and irregular nanowires, these films have been synthesized using an anodization process in a fluoride-based EG electrolyte. This behavior might be caused by the incomplete removal of electrolyte, which brought carbon impurities to the surface of the nanowires and irregular nanowires samples during the annealing process.

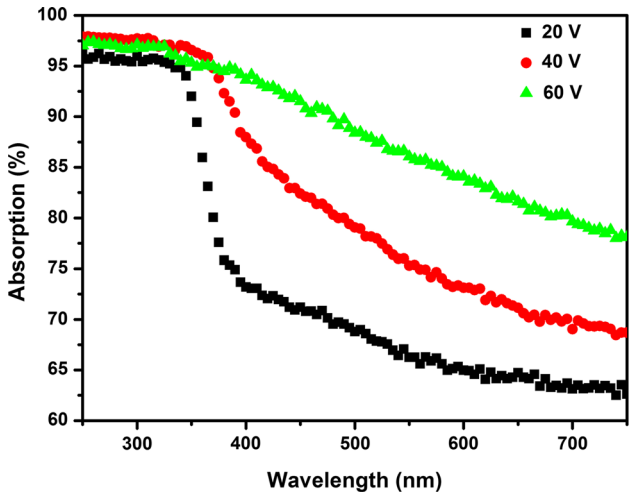

Fig. 5. UV–Vis absorption spectra of TiO_2 NTs with nanograss layer.

To calculate the optical band gap of TiO_2 NTs with nanograss layer; Figure 6 shows the plots of $(\alpha h\upsilon)^2$ versus photon energy ($h\upsilon$), and the extrapolation of the straight line to zero absorption gives the effective band gap energy (E_g) value. It was found that the band gap of the samples decreased if the anodization voltage increased, taking values of 3.04 eV, 2.63 eV and 2.25 eV for 20 V, 40 V and 60 V, respectively. This could be due to the increase of specific surface area with the formation of a nanograss layers for films prepared at 20 V and 40 V. However, in terms of nanograss, the additional large surface area offers new light trapping sites which may improve the optical performance of TiO_2 NTs to some extent. Furthermore, we suggest this behavior is due to the presence of defects producing additional states at the band gap near the conduction band (CB) or the valence band (VB). These material defects may be oxygen vacancies and/or titanium interstitials, thus altering the electrical and optical properties of the material. Moreover, the presence of rutile phase is noted at high anodizing voltages for TiO_2 NTs, as compared with the anatase phase for TiO_2 NTs with nanograss structures at lower voltages. The difference in crystallization may be due to a quantization effect of the structure resulting from the presence of the nanograss form which can cause a high degree of lattice distortion compared to TiO_2 NTs films without nanograss, where the band gap decreases to 2.25 eV providing extended absorption into visible region. Sun et al.[54] reported the growth of TiO_2 nanostructure arrays from nanorods (NRODs) to nanoribbons (NRIBs), and then nanowires (NWs) by a simple hydrothermal treatment with the assistance of a surfactant. Different band gap values were obtained, namely 3.0, 3.07 and 3.25 eV for NRODs, NRIBs and NWs, respectively attributed to

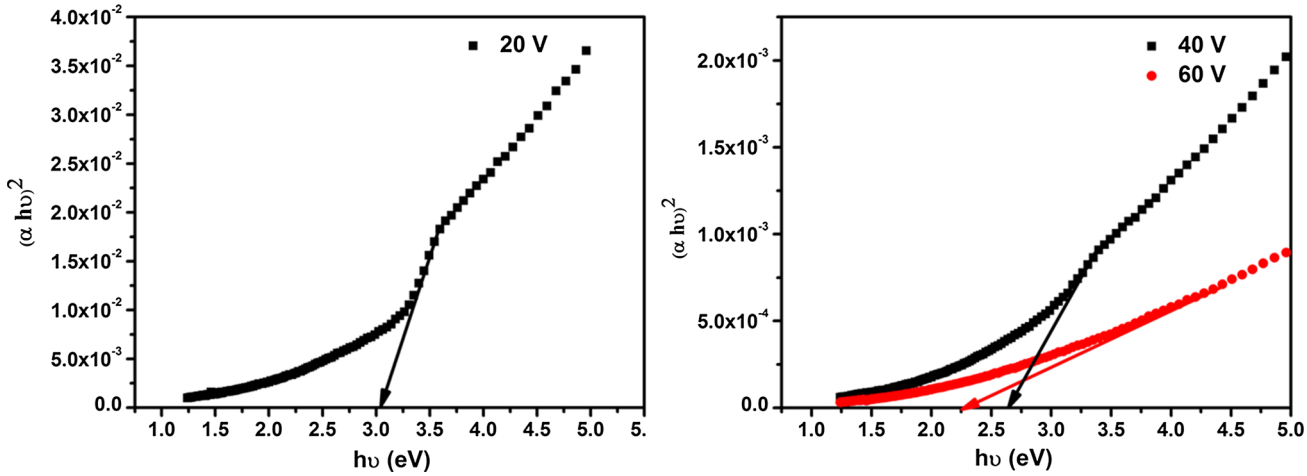

Fig. 6. Graph of $(\alpha h\upsilon)^2$ versus photon energy ($h\upsilon$) for different TiO_2 NTs with nanograss layers.

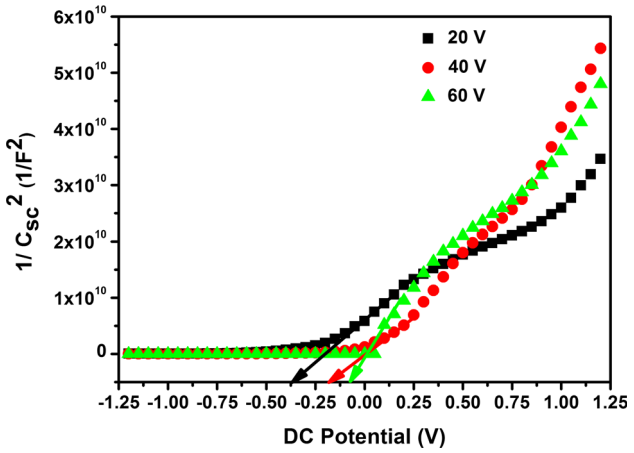

Fig. 7. MS plots of the TiO_2 NTs with nanograss layer prepared by varying the applied voltage.

the quantum-size effect and possible difference in Fermi energies.

Semiconducting Properties

MS analysis was performed for the amorphous TiO_2 NTs with nanograss layers. Figure 7 displays the MS plots for these films. All curves show a positive slope indicating the *n* type semiconducting nature of the different nanostructured films. The donor density N_d can be determined using the following MS relation[39]:

$$N_d = \frac{2}{e\varepsilon\varepsilon_0 s}, \quad (7)$$

where *s* is the positive slope of each straight line in the MS plots. Table I summarizes the electronic properties of amorphous TiO_2 nanostructured films. It noticeable that N_d increases towards higher values upon increasing the anodizing voltage until

Table I. The semiconductor properties of TiO_2 NTs with nanograss layers prepared by varying the applied voltage

Applied voltage (V)	N_d (cm^{-3})	U_{fb} (V)
20	1.14×10^{21}	− 0.38
40	2.15×10^{21}	− 0.17
60	1.65×10^{21}	− 0.07

40 V. In fact N_d of the as-prepared TiO_2 NTs at 20 and 40 V are 1.14×10^{21} cm^{-3} and 2.15×10^{21} cm^{-3}, respectively, while the value for film synthesized at 60 V shows a small decrease to 1.65×10^{21} cm^{-3}. Since there is a change in the nanotube morphology with anodization voltage evidenced by nanograss appearance at lower anodization voltage (20 V and 40 V), the increase in the donor density up to 40 V could be associated to more disordered amorphous films with an increase in the defects presented in the lattice. So, the existence of a nanograss layer provides supplementary abundant local donor energy levels; the charge transport is significantly improved along the TiO_2 NTs by increasing the number of defects.[55] In addition, the curves show the existence of a second linear region over a wide range of potentials, explained by the ionization of deeper states in the TiO_2 NTs films. However, deep defects can release charge carriers by thermal excitation. Furthermore, the decrease of N_d value at 60 V indicates diminution of defects present in the material. Acevedo-Peña et al.[56] revealed the effect of anodization voltage and time on semiconducting properties of TiO_2 NTs. Different dependences were obtained exhibiting the various defects formed in the TiO_2 lattice during the anodization process. Moreover, Roy et al.[41] described an improvement of fluorine ion insertion into TiO_2 layers by increasing the anodization voltage. So, the high N_d values for amorphous

TiO_2 NTs can be related to the large insertion of fluoride ions.[57]

The flat band potential (U_{fb}) can also be calculated from the MS plots. This potential is defined as that which must be applied at the electrode/electrolyte interface in order to cancel the flexion of the energy bands (Schottky barrier) and to align the Fermi levels. In addition, the U_{fb} is related to the space charge layer potential (U_{sc}) which developed inside the semiconductor when it is in contact with the electrolyte or a metal and the external potential (U) of the junction according to the equation

$$U_{sc} = U - U_{fb}. \quad (8)$$

For a given value of U, a higher and more negative value of U_{fb} corresponds to a higher and more positive value of U_{sc} translating to a stronger internal electric field allowing a better separation of the electric charges (electron–hole), thus reducing the recombination rate.[58–61]

From MS plots, the extrapolation of the straight line to the abscissa axis (the potential axis) gives the U_{fb} potential value. By increasing the anodizing voltage, U_{fb} takes less negative values. Indeed, the U_{fb} values are − 0.38, − 0.17 and − 0.07 V for films prepared at 20, 40 and 60 V respectively. This behavior can be attributed to a shift of the Fermi level towards the conduction band edge since it is an n-type semiconductor, which indicates a lower recombination probability for films prepared at 20 V with a nanograss appearance. In the same context, Yahia et al.[62] obtained similar behavior of flat band potential variation with increasing anodization voltages in frequency dependence measurements.

CONCLUSION

TiO_2 NTs covered with nanograss were successfully synthesized following a potentiostatic anodization process by varying the applied voltage. At voltages of 20 and 40 V, nanograss layers were formed following the formation of beams from the bending and collapse of tube walls after inhomogeneous distribution of fluoride ions that generates an electrochemical etching gradient. The mechanism formation of nanograss over the TiO_2 NTs surface was described based on a vertical splitting model. While under rapid potentiostatic anodization at 60 V, nanotubular morphology was significantly improved, and the nanograss aspect was eliminated due to the favoring of fluoride ion diffusion, thus preventing the formation of cracks. Moreover, the n-type semiconductor nature of anodized samples displays a higher N_d value with applied voltage until 40 V, indicating supplementary defects present in the lattice subsequent to the increase in specific surface area with nanograss formation. In addition, the U_{fb} has a more negative value indicating a lower recombination probability for the film prepared at 20 V with a nanograss appearance. Furthermore, heat treatment of the film prepared at 60 V yields an absorption band extending up to 400 nm in wavelength, corresponding to a band gap of 2.25 eV, due to quantum size effects with the apparition of the rutile phase and the possible existence of new states in the band gap.

ACKNOWLEDGMENTS

The authors thank Dr. Thomas WOOD (University of Lyon) for the time and interest in improving the paper. This work is carried out with the contribution of the cooperation Project No. 16 MDU 970, Mixed Evaluation and Prospective Commission—Hubert Curien Program (CMEP-PHC) TASSILI.

CONFLICT OF INTEREST

The authors declare that they have no conflicts of interest.

REFERENCES

1. M. Morozova, P. Kluson, J. Krysa, M. Vesely, P. Dzik, and O. Solcova, *Procedia Eng.* 42, 573 (2012).
2. J. Reszczyńska, T. Grzyb, J.W. Sobczak, W. Lisowski, M. Gazda, B. Ohtani, and A. Zaleska, *Appl. Surf. Sci.* 307, 333 (2014).
3. P. Pungboon Pansila, N. Witit-anun, and S. Chaiyakun, *Procedia Eng.* 32, 862 (2012).
4. D.V. Bavykin, J.M. Friedrich, and F.C. Walsh, *Adv. Mater.* 18, 2807 (2006).
5. N. Liu, X. Chen, J. Zhang, and J.W. Schwank, *Catal. Today* 225, 34 (2014).
6. H. Li, Q. Zhou, Y. Gao, X. Gui, L. Yang, M. Du, E. Shi, J. Shi, A. Cao, and Y. Fang, *Nano Res.* 8, 900 (2015).
7. D. Khudhair, A. Bhatti, Y. Li, H. Amani Hamedani, H. Garmestani, P. Hodgson, and S. Nahavandi, *Mater. Sci. Eng. C* 59, 1125 (2016).
8. Y. Zhang, D. Yu, M. Gao, D. Li, Y. Song, R. Jin, W. Ma, and X. Zhu, *Electrochim. Acta* 160, 33 (2015).
9. Q. Cai, M. Paulose, O. Varghese, and C. Grimes, *J. Mater. Res.* 20, 230 (2005).
10. A. Hazra, K. Dutta, B. Bhowmik, V. Manjuladevi, R.K. Gupta, P.P. Chattopadhyay, and P. Bhattacharyya, *J. Electron. Mater.* 43, 3229 (2014).
11. J. Song, X. Zhang, C. Zhou, Y. Lan, Q. Pang, and L. Zhou, *J. Electron. Mater.* 44, 22 (2015).
12. Y.L. Pang, S. Lim, H.C. Ong, and W.T. Chong, *Appl. Catal. A* 481, 127 (2014).
13. M. Assefpour-Dezfuly, C. Vlachos, and E.H. Andrews, *J. Mater. Sci.* 19, 3626 (1984).
14. V. Zwilling, M. Aucouturier, and E. Darque-Ceretti, *Electrochim. Acta* 45, 921 (1999).
15. D. Gong, C. Grimes, O. Varghese, W. Hu, R. Singh, Z. Chen, and E. Dickey, *J. Mater. Res.* 16, 3331 (2001).
16. J. Macák, H. Tsuchiya, and P. Schmuki, *Angew. Chemie. Int. Ed.* 44, 2100 (2005).
17. J. Macak, H. Tsuchiya, L. Taveira, S. Aldabergerova, and P. Schmuki, *Angew. Chemie. Int. Ed.* 44, 7463 (2005).
18. J. Macák, H. Tsuchiya, A. Ghicov, and P. Schmuki, *Electrochem. Commun.* 7, 1133 (2005).
19. J. Liang, G. Zhang, Y. Yang, and J. Zhang, *J. Mater. Chem. A.* 2, 19841 (2014).
20. J. Yan and F. Zhou, *J. Mater. Chem.* 21, 9406 (2011).
21. R. Sánchez-Tovar, I. Paramasivam, K. Lee, and P. Schmuki, *J. Mater. Chem.* 22, 12792 (2012).
22. R. Lü, W. Zhou, K. Shi, Y. Yang, L. Wang, K. Pan, C. Tian, Z. Ren, and H. Fu, *Nanoscale* 5, 8569 (2013).

23. M. Kalbacova, J.M. Macak, F. Schmidt-Stein, C.T. Mierke, and P. Schmuki, *Phys. Status Solidi RRL* 2, 194 (2008).
24. Z. Liu, X. Zhang, S. Nishimoto, T. Murakami, and A. Fujishima, *Environ. Sci. Technol.* 42, 8547 (2008).
25. J. Kong, Y. Wang, Q. Sun, and D. Meng, *J. Electron. Mater.* 46, 4791 (2017).
26. M. Xia, L. Huang, Y. Zhang, and Y. Wang, *J. Electron. Mater.* 47, 5291 (2018).
27. K.M. Kummer, E.N. Taylor, N.G. Durmas, K.M. Tarquinio, B. Ercan, and T.J. Webster, *J. Biomed. Mater. Res. B* 101, 677 (2013).
28. F. Mohammadpour and M. Moradi, *Mater. Sci. Semicond. Process.* 39, 255 (2015).
29. J. Naduvath, P. Bhargava, and S. Mallick, *Chem. Phys. Lett.* 626, 15 (2015).
30. J.H. Lim and J. Choi, *Small* 3, 1504 (2007).
31. C. Zhang, J. Xing, H. Fan, W. Zhang, M. Liao, and Y. Song, *J. Mater. Sci.* 52, 3146 (2017).
32. D. Wang, L. Liu, F. Zhang, K. Tao, E. Pippel, and K. Domen, *Nano Lett.* 11, 3649 (2011).
33. S. Zhao, Y. Chen, Z. Zhao, L. Jiang, C. Zhang, J. Kong, and X. Zhu, *Electrochim. Acta* 266, 233 (2018).
34. K. Du, G. Liu, M. Li, C. Wu, X. Chen, and K. Wang, *Electrochim. Acta* 210, 367 (2016).
35. M. Michalska-Domańska, P. Nyga, and M. Czerwiński, *Corros. Sci.* 134, 99 (2018).
36. Y. Sun and K.P. Yan, *Int. J. Hydrogen Energy* 39, 11368 (2014).
37. S. Liu, J. Yu, and M. Jaroniec, *Chem. Mater.* 23, 4085 (2011).
38. Y.S. Sohn, Y.R. Smith, M. Misra, and V.R. Subramanian, *Appl. Catal. B* 84, 372 (2008).
39. P. Acevedo-Peña, J.E. Carrera-Crespo, F. González, and I. González, *Electrochim. Acta* 140, 564 (2014).
40. K. Zhu, T.B. Vinzant, N.R. Neale, and A.J. Frank, *Nano Lett.* 7, 3739 (2007).
41. P. Roy, S. Berger, and P. Schmuki, *Angew. Chem. Int. Ed.* 50, 2904 (2011).
42. Y. Xue, Y. Sun, G. Wang, K. Yan, and J. Zhao, *Electrochim. Acta* 155, 312 (2015).
43. V. Galstyan, A. Vomiero, E. Comini, G. Faglia, and G. Sberveglieri, *RSC Adv.* 1, 1038 (2011).
44. A.F. Kanta, M. Poelman, and A. Decroly, *Sol. Energy Mater. Sol. Cells* 133, 76 (2015).
45. D. Khudhair, H.A. Hamedani, J. Gaburro, S. Shafei, S. Nahavandi, H. Garmestani, and A. Bhatti, *Mater. Sci. Eng. C* 77, 111 (2017).
46. Z. Wu, S. Guo, H. Wang, and Y. Liu, *Electrochem. Commun.* 11, 1692 (2009).
47. J. Wang and Z. Lin, *Chem. Mater.* 20, 1257 (2008).
48. A. Haring, A. Morris, and M. Hu, *Materials* 5, 1890 (2012).
49. S. Berger, S.P. Albu, F. Schmidt-Stein, H. Hildebrand, P. Schmuki, J.S. Hammond, D.F. Paul, and S. Reichlmaier, *Surf. Sci.* 605, L57 (2011).
50. O.K. Varghese, D. Gong, M. Paulose, C.A. Grimes, and E.C. Dickey, *J. Mater. Res.* 18, 156 (2003).
51. J. Zhao, X. Wang, T. Sun, and L. Li, *J. Alloys Compd.* 434, 792 (2007).
52. Z. Lockman, S. Sreekantan, S. Ismail, L. Schmidt-Mende, and J.L. MacManus-Driscoll, *J. Alloys Compd.* 503, 359 (2010).
53. R.S. Mane, W.J. Lee, H.M. Pathan, and S.H. Han, *J. Phys. Chem. B* 109, 24254 (2005).
54. Z. Sun, J.H. Kim, T. Liao, Y. Zhao, F. Bijarbooneh, V. Malgras, and S.X. Dou, *CrystEngComm* 14, 5472 (2012).
55. S. Palmas, A.M. Polcaro, J.R. Ruiz, A. Da Pozzo, M. Mascia, and A. Vacca, *Int. J. Hydrogen Energy* 35, 6561 (2010).
56. P. Acevedo-Peña and I. González, *Procedia Chem.* 12, 34 (2014).
57. B. Munirathinam and L. Neelakantan, *J. Electroanal. Chem.* 770, 73 (2016).
58. J. Borràs-Ferrís, R. Sánchez-Tovar, E. Blasco-Tamarit, R.M. Fernández-Domene, and J. Garcia-Anton, *Electrochim. Acta* 196, 24 (2016).
59. M. Radecka, M. Rekas, A. Trenczek-Zajac, and K. Zakrzewska, *J. Power Sources* 181, 46 (2008).
60. R. Sánchez-Tovar, R.M. Fernández-Domene, D.M. García-García, and J. García-Antón, *J. Power Sources* 286, 224 (2015).
61. D. Wang, X. Zhang, P. Sun, S. Lu, L. Wang, C. Wang, and Y. Liu, *Electrochim. Acta* 130, 290 (2014).
62. S. Ait Ali Yahia, L. Hamadou, A. Kadri, N. Benbrahim, and E.M.M. Sutter, *J. Electrochem. Soc.* 159, K83 (2012).